Doping concentration driven morphological evolution of Fe doped ZnO nanostructures

A. Sahai, Y. Kumar, V. Agarwal, S.F. Olive-Méndez and N. Goswami

Abstract

In this paper, systematic study of structural, vibrational, and optical properties of undoped and 1-10 at.% Fe doped ZnO nanostructures, synthesized adopting chemical precipitation route, has been reported. Prepared nanostructures were characterized employing an assortment of microscopic and spectroscopic techniques, namely Scanning Electron Microscopy (SEM), Transmission Electron Microscopy (TEM), Energy Dispersive X-ray (EDX) Spectroscopy, X-ray Diffraction (XRD), Fourier Transform Infrared (FTIR), Micro-Raman Spectroscopy (μRS), and UV-visible and Photoluminescence (PL) spectroscopy. With Fe incorporation, a gradual morphological transformation of nanostructures is demonstrated vividly through SEM/TEM characterizations. Interestingly, the morphology of nanostructures evolves with 1–10 at. % Fe doping concentration in ZnO. Nanoparticles obtained with 1 at. % Fe evolve to nanorods for 3 at. % Fe; nanorods transform to nanocones (for 5 at. % and 7 at. % Fe) and finally nanocones transform to nanoflakes at 10 at. % Fe. However, at all these stages, concurrence of primary hexagonal phase of $Zn_{1-x}Fe_xO$ along with the secondary phases of cubic $ZnFe_2O_4$ and rhombohedric Fe_2O_3, is revealed through XRD analysis. Based on collective XRD, SEM, TEM, and EDX interpretations, a model for morphological evolution of nanostructures was proposed and the pivotal role of Fe dopant was deciphered. Furthermore, vibrational properties analyzed through Raman and FTIR spectroscopies unravel the intricacies of formation and gradual enhancement of secondary phases with increased Fe concentration. UV-visible and PL spectroscopic analyses provided further insight of optical processes altering with Fe incorporation. The blue shift and gradual quenching of visible photoluminescence with Fe doping was found in accordance with structural and vibrational analyses and explicated accordingly.

Introduction

Based on the research till date, zinc oxide (ZnO) has proven to be a uniquely versatile metal oxide semiconductor. [1–6] Importance of ZnO is majorly due to its vast applications founded on diverse fundamental properties.[1,5–14] For example, ZnO crystallizes in the wurtzite structure at atmospheric pressure and transits to the rock-salt structure at about 9 GPa.[8] Consequently, rock-salt ZnO is an indirect semiconductor with a band gap of 2.45±0.15 eV, whereas wurtzite structure ZnO usually has direct band gap of 3.37 eV at room temperature with a large exciton binding energy of 60 meV and hence, enabling excitonic-related device applications.[7,8] Advantages associated with a large band gap further include higher breakdown voltages, ability to sustain large electric fields, lower electronic noise, high temperature and high power operation and efficient photo-catalytic hybrid nanostructures for hydrogen generation.[11,15,16] ZnO is the most suitable semiconductor with excellent optical, electronic, and even multiferroic properties that make it versatile for numerous diverse applications such as, solar cells, field effect transistors, gas sensors, phosphor and piezoelectric applications, etc.[5,17,18]

It is well established now that owing to quantum confinement effects and enhanced surface to volume ratio, nanosize semiconductors exhibit advanced properties as compared to their bulk counterparts.[9–12] The synthesis and properties of assorted ZnO nanostructures (e.g., nanoparticles, nanorods, nanowhiskers, nanoflowers, etc.) are therefore frequently reported.[7,9–14] The doping of ZnO nanostructure with transition metal is an effective approach to engineer the energy levels and surface states and hence drastically alter its properties. [5,15,19–21] However, production of transition metal doped ZnO nanostructures employing facile, high yield yet low cost synthesis processes is still challenging.[19] Pure phase synthesis of oxide nanomaterials is often accomplished by expensive techniques namely, molecular beam epitaxy, RF sputtering, pulse laser deposition, chemical vapor deposition, etc.[1] Owing to the interface between growth layer and substrate, amorphous materials are usually produced through these methods and an additional high-temperature/high-vacuum processing step is required to obtain crystalline phase.[1] But high temperature processes may lead to significant sideeffects, for example, formation of multiple phases.[1] In this context, chemical precipitation method is a facile technique with high throughput and pure phase synthesis of undoped and doped ZnO nanostructures and therefore, employed here to prepare Fe doped ZnO nanostructures.[10–12,19]

Recently, structural transformation of nanoparticles to nanorods caused by doping of nickel in ZnO is also reported.[19] Although structural transformation is observed for various doped semiconductors, there are fewer reports detailing dopant concentration dependent morphological evolution of ZnO nanostructures.[22–25] Nonetheless, in order to systematically investigate dopant concentration driven structural transformation, it is crucial to know the values of solubility limit of transition metal (e.g., Fe in present article) doping in ZnO and also ascertain the role of dopant in formation of additional phases; as these factors directly affect the process of structural transformation as well as optical, spintronic applications, etc.[25–27] As per published data, the highest solubility limits for transition elements namely, Co, Mn, Fe, and Ni in ZnO are found to be 30%, 30%, 20%, and 3% (at. wt.), respectively.[26] However, in another report on Fe doped ZnO structures grown via different methods, the solubility of iron found to be in the range of 0.4–1 at. %.27 In view of variation in the reported values of Fe solubility limit, it could be of interest to probe the solubility of Fe in ZnO nanostructures.

Experimental details

Fe-doped ZnO nanostructures were prepared adopting the chemical precipitation route.[19] Procedure and mechanism of the synthesis in principle is similar to the one reported earlier for Ni doped ZnO nanostructures.[19] In order to prepare Fe-doped ZnO nanostructures, the precursors used are: $Zn(CH_3COO)_2.2H_2O$ (Aldrich, 99.999% purity), NaOH (Sigma-Aldrich, ≥98% purity), Fe_2O_3 (Alrdich, purity≥99.00%). All the reactant chemicals were used as received without any processing. In the synthesis process, Fe_2O_3 powder was used to obtain different molar concentrations of doping namely, 1 at. %, 3 at. %, 5 at. %, 7 at. %, and 10 at. % of Fe in ZnO. As per desired Fe doping concentration, the estimated aliquot of Fe_2O_3 solution was added to a solution of $Zn(CH_3COO)_2.2H_2O$. In this base solution, NaOH solution was added drop wise. During the entire process, magnetic stirring was carried out to achieve the precipitate of Fe doped ZnO nanostructures. This precipitate of Fe doped ZnO was thoroughly washed with de-ionized water to discard residual by-products. Then precipitate was dried at 200 °C for 6 h. The dried precipitate was ground and annealed at 400 °C for 2 h to further remove the impurities of carbonates, etc. Finally, Fe doped ZnO powder is ground for further investigations. More details of procedure and mechanism of nanophase formation employing chemical precipitation method can be found elsewhere.[10,19,28,29]

Characterization

The shape, size, and distribution of nanostructures were investigated employing high resolution JEOL JSM-7401F FESEM and JEOL JEM-2200FS TEM with spherical aberration corrector (Cs) for STEM mode. Utilizing this instrument, Energy Dispersive X-ray (EDX) analysis was performed and chemical composition was quantified using INCA software. A Xpert'PRO X-ray Diffraction (XRD) spectrometer, equipped with Cu anode X-ray tube (with Kα radiation of 1.54Å), a flat crystal monochromator, and a proportional detector consisting of a cylindrical chamber filled with xenon/methane gas mixture, was used to record characteristic X-ray diffraction patterns of prepared nanostructures. To obtain information about the possible bonds formation in prepared material, a Cary 660 Fourier transform infrared (FTIR) spectrophotometer was used to record vibrational modes. To probe inelastic scattering processes in prepared material, room temperature Raman spectra were collected using a Jobin Yvon RAM HR 800 spectrophotometer with Olympus BX41 microscope and a CCD detector. The 632.8 nm emission of He-Ne laser was used here as an excitation source. Band gap measurements were performed using Shimadzu (model UV3010) UV–visible–NIR spectrophotometer coupled with an integrating sphere. Finally, excitation wavelength of 325 nm from a xenon lamp of Varian Fluorescence spectrometer (Cary Eclipse) was employed to study the steady state Photoluminescence (PL) properties of prepared nanostructures.

Result and discussion

Scanning electron microscopy (SEM) analysis: Direct measurement of morphological features of prepared nanostructures was performed through SEM analysis. Real space SEM images of undoped ZnO and 1–10 at. % Fe doped ZnO nanostructures are shown in Figure [1]. A glimpse of SEM images vividly indicates the transformation of ZnO nanostructures with variation in Fe doping concentration. In order to thoroughly probe the cause and pattern of this transformation, we carefully analyze the alterations in morphological features of 1–10 at. % Fe doped ZnO nanostructures. The irregular shaped nanoparticles of 100 nm average size (Figure 1(a)) are clearly observed for undoped ZnO. Coalescence of such 100 nm size nanoparticles results in formation of larger agglomerates. Similar to undoped ZnO, irregular shaped 100 nm nanoparticles are seen for 1 at. % Fe doped ZnO and therefore, influence of Fe doping on size or shape is not apparent from SEM image at this stage (Figure 1(b)). For 3 at. % Fe, hexagonal rods of approximately 1 μm long and 500 nm edge length are observed in Figure 1(c). In fact, onset of structural transformation is evident for 3 at. % Fe. At this stage, enhanced Fe doping induced anisotropic growth not only causes the formation of hexagonal rods but here onwards, the evolution of prismatic shapes initiates. As marked through dashed lines in Figure 1(c), the prismatic structure comprises the hexagonal base of 500 nm edge length and hexagonal shape tip of 250 nm edge length. The systematic transformation continues with further Fe doping and vividly evident for 5, 7, and 10 at. % Fe doped ZnO nanostructures, as shown respectively through Figures 1(d)–1(f). As seen in the inset and main Figure 1(d), formation of prismatic nanocones completes for 5 at.b% Fe doping.

These cones are formed probably via evolution of truncated prismatic hexagon, as hinted previously for 3 at. % Fe (in Figure 1(c)). The formation of nanocones with 1 lm slant length and well defined morphology is indeed complete at this stage. Considering the growth pattern of Fe doped ZnO nanostructures till now, we may suggest that the anisotropic growth of ZnO lattice along one particular crystallographic axis (say c-axis) causes the transformation of nanoparticles (1 at. % Fe) into hexagonal structures (3 at. % Fe).

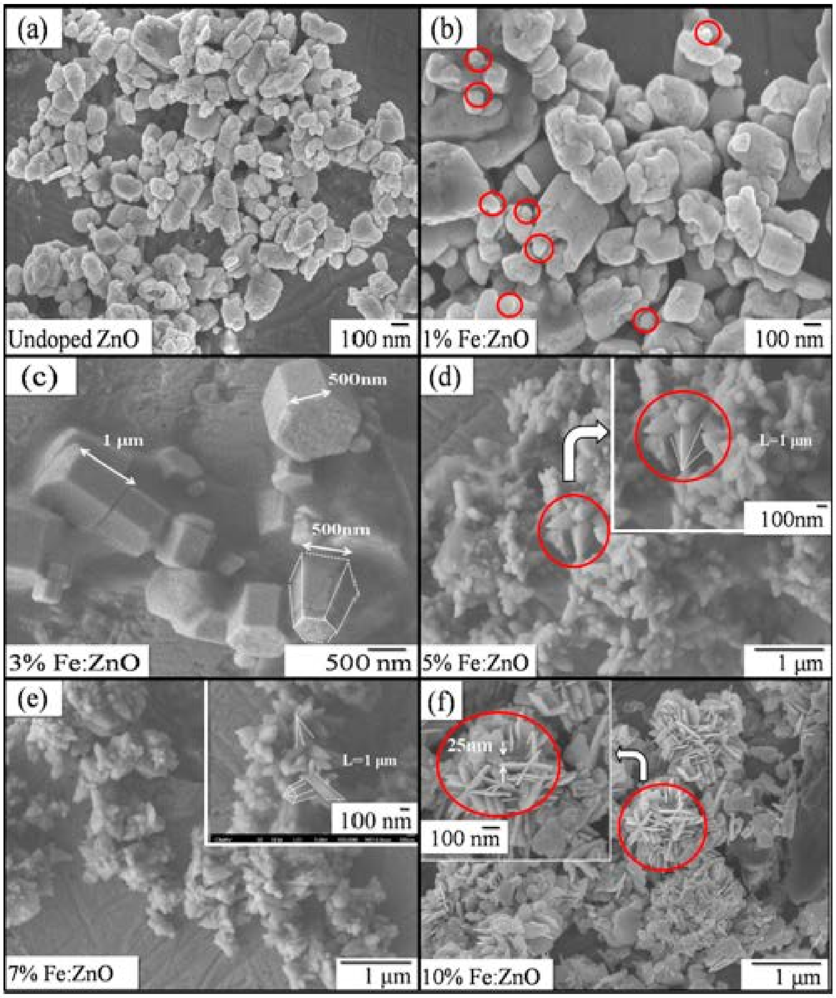

FIG. 1. SEM images for (a) undoped ZnO, (b) 1 at. %, (c) 3 at. %, (d) 5 at. %, (e) 7 at. %, and (f) 10 at. % Fe doped ZnO nanostructures.

With enhanced Fe doping (5 at. % Fe), the sharpening of one side of hexagonal rods along c-axis results in construction of prismatic nanocones. However, the growth along c-axis weakens with further increase of doping concentration. As shown in Figure 1(e), the c-axis growth could not be sustained for 7 at. % Fe doping and therefore triggers the rupturing of conical shapes. As seen in inset of Figure 1(e), with increased Fe doping (7 at. %), nanocones start becoming unstable and hence, instead of c-axis anisotropic growth, now growth initiates in other axes (say a and b axes) at this stage and get prominent afterwards. The dominant planar growth of structure (along a and b axes) for 10 at. % Fe doping is demonstrated clearly through the build-up of approximately 500 nm long and ~25 nm thick sheet type structures of “nanoflakes,” as exhibited in Figure 1(f). No other shape, but bunches of nanoflakes, are seen at this stage. Thus, SEM analysis of 1–10 at. % Fe doped ZnO nanostructures directly demonstrates the morphological evolution of nanoparticles to hexagonal rods transforming into prismatic nanocones and finally to nanoflakes. However, the growth of various morphologies of nanostructures could be explained partly on the basis of SEM analysis. EDX and TEM characterizations were therefore performed to get further insight of morphological evolution.

Energy dispersive x-ray spectroscopy and transmission electron microscopy (TEM) analysis: EDX spectroscopy was performed to determine the chemical compositions of prepared nanostructures. TEM images, utilized for EDX analysis of 1, 5, and 10 at. % Fe doped ZnO nanostructures, are shown as Figures 2, 3(a), and 4(a), respectively. Also, in order to locate the position of Fe dopant in ZnO and quantify Fe concentration in 5 at. % and 10 at. % Fe doped ZnO; elemental mappings for fundamental constituents (i.e., Zn, O, Fe) are presented through Figures 3(b)–3(d) and Figures 4(b)–4(d), respectively.

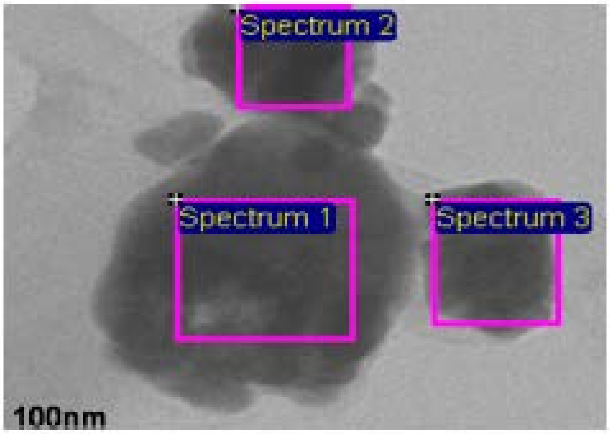

FIG. 2. TEM image of 1 at. % Fe doped ZnO nanoparticles.

It is evident from Figures 3 and 4 that superposition of elemental mapping profiles of individual constituents matches with the respective TEM images. It could be an interesting observation in Figure 3 that the tip points of nanostructures are always occupied by Fe atom. Moreover, these profiles confirm the uniform dispersion of Fe atoms into ZnO and the regions where higher Fe concentration is observed (Figure 4(d)) may indicate the formation of secondary phase due to excess of Fe. The quantitative analysis of 1 at. %, 5 at. %, and 10 at. % Fe doped ZnO is presented in Table I.

It is evident from these calculations that Fe doping does occur in synthesized nanostructures, as the estimated quantity of dopant found to match the order of theoretically expected value of dopant concentration. Nevertheless, the concentrations of Zn and Fe defects vary with doping concentration and hence suggest probable formation of some secondary phase (such as $ZnFe_2O_4$, Fe_2O_3), in addition to typical primary phase of $Zn_{1-x}Fe_xO$. Furthermore, excess Fe impurity, unutilized for doping, could possibly assist in growth and morphological evolution of nanostructures. However, for quantitative estimation of Fe assisted formation of primary and secondary phases (if any) and more importantly to ascertain the role of Fe in morphological evolution of nanostructures, a detailed systematic XRD study is essential and hence performed.

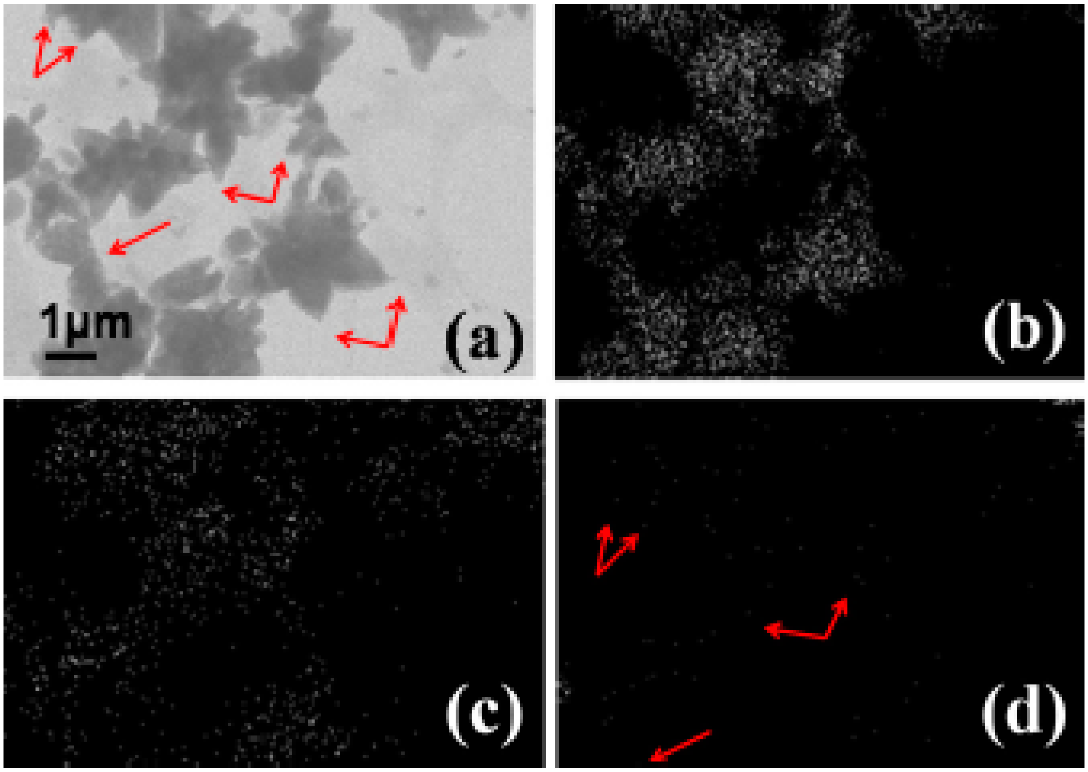

FIG. 3. (a) TEM image of 5 at. % Fe doped ZnO. Elemental mapping depicting the distribution of constituents (b) Zn($K\alpha_1$), (c) O($K\alpha_1$), and (d) Fe($K\alpha_1$). The location of Fe atoms at the tip point in TEM image and their corresponding position in elemental mapping image are indicated by the arrows.

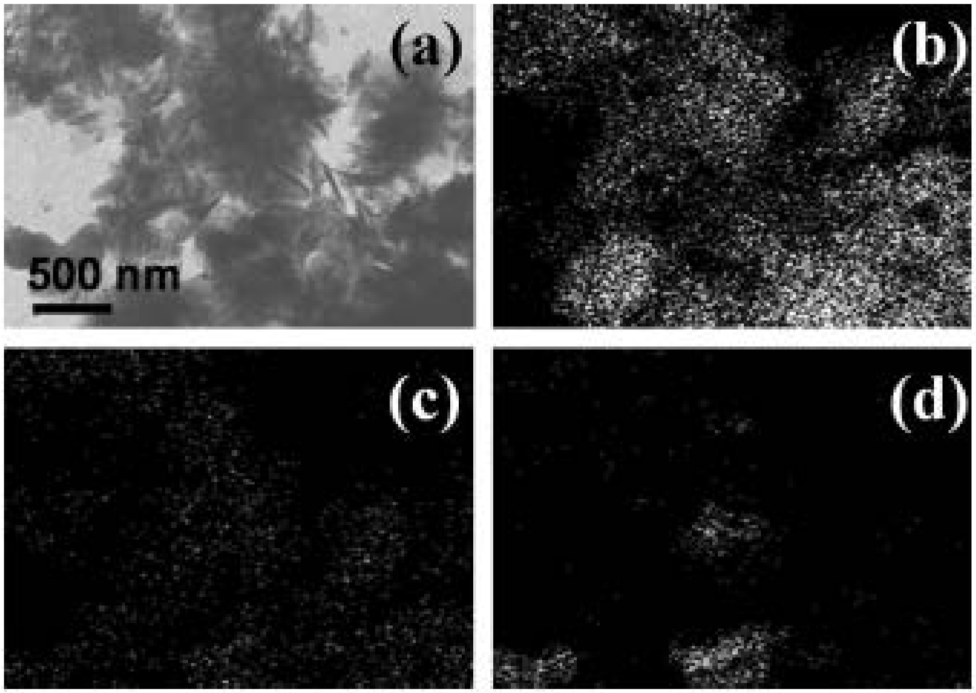

FIG. 4. TEM image of 10 at. % Fe doped ZnO. Elemental mapping depicting the distribution of constituents (b) Zn(Kα_1), (c) O(Kα_1), and (d) Fe(Kα_1).

X-ray diffraction analysis: The crystallographic interpretations based on XRD data could provide significant information about formation of phase(s) for 1–10 at. % Fe doped ZnO nanostructures and their structural transformation. Aiming this, the XRD patterns of undoped and Fe-doped nanostructures were recorded, as presented in Figure 5.

In close agreement with the standard data (JCPDS file no. 36–1451), XRD data reveal that prepared Fe-doped nanostructures possess wurtzite phase of ZnO.[10] The prominent lattice planes observed for 1–10 at. % Fe doped ZnO nanostructures are: (100), (002), (101), (102), (110), (103), (200), (112), (201), (004), and (202). These characteristic lines, respectively, at 31.6°, 34.2°, 36.1°, 47.3°, 56.3°, 62.7°, 66.2°, 67.5°, 68.8°, 72.6°, 77.0°, are marked with “Δ” in Figure 5.[10–12,19,30] This confirms that hexagonal phase of ZnO phase is retained by Zn1-xFexO phase of 1–10 at. % Fe doped ZnO.

Having ascertained primary $Zn_{1-x}Fe_xO$ phase, we now examine the possible occurrence of other additional phases. As seen in the main and inset Figure 5(i), a peak at 44.5° is vividly observed for 7 at. % and 10 at. % Fe doped samples. This peak does not belong to XRD characteristic spectrum of ZnO and actually correspond to (400) plane of cubic $ZnFe_2O_4$ phase.[30] Other planes of $ZnFe_2O_4$ phase are (220), (311), (511), and (440).30 These planes, respectively at 31.5°, 36.1°, 56.5°, and 62.5°, are observed for all 1–10 at. % Fe doped ZnO and marked as "*" in Figure 5. It is notable here that broadening of peaks actually results from the convolution of (220), (311), (511) and (440) planes of $ZnFe_2O_4$ phase concurring with the (100), (101), (110), and (103) XRD lines of Zn1-xFexO phase.

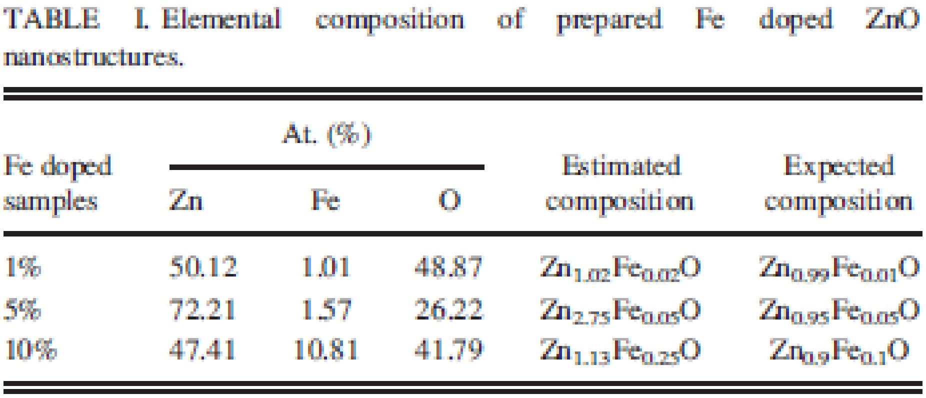

TABLE I. Elemental composition of prepared Fe doped ZnO nanostructures.

Fe doped samples	At. (%)			Estimated composition	Expected composition
	Zn	Fe	O		
1%	50.12	1.01	48.87	$Zn_{1.02}Fe_{0.02}O$	$Zn_{0.99}Fe_{0.01}O$
5%	72.21	1.57	26.22	$Zn_{2.75}Fe_{0.05}O$	$Zn_{0.95}Fe_{0.05}O$
10%	47.41	10.81	41.79	$Zn_{1.13}Fe_{0.25}O$	$Zn_{0.9}Fe_{0.1}O$

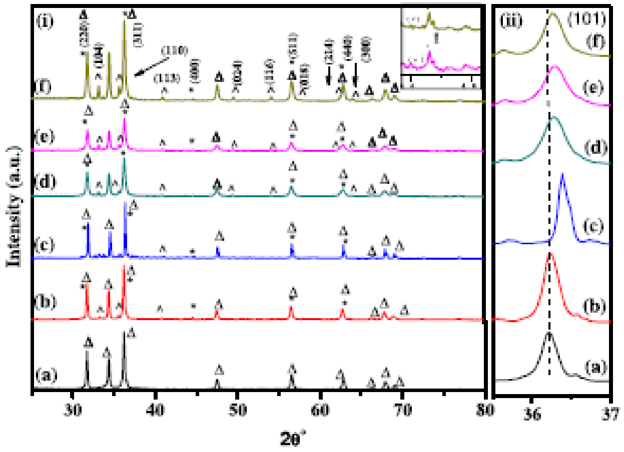

FIG. 5. (i) XRD pattern of (a) undoped, (b) 1 at. %, (c) 3 at. %, (d) 5 at. % (e) 7 at. %, and (f) 10 at. % Fe doped ZnO nanostructures. In the inset enlarged view of XRD scan around 44.5° is shown for 7 at. % and 10 at. % Fe doping. The peak positions pertaining to $Zn_{1-x}Fe_xO$, $ZnFe_2O_4$ and Fe_2O phases are labeled respectively through symbols Δ, *, and ^. (ii) Shifting o (101) peak for respective nanostructures.

This implies that the formation of secondary phase of $ZnFe_2O_4$ (JCPDS file no. 22–1012), in addition to the primary ZnO phase of $Zn_{1-x}Fe_xO$, takes place for all Fe concentrations. However, (400) plane of ZnFe2O4 at 44.5° is observed distinctly for 7 at. % (Figure 5 i(e)) and 10 at. % Fe doped ZnO (Figure 5 i(f)). This suggests that formation of cubic $ZnFe_2O_4$ phase actually gets prominent with increased Fe doping.[30]

The diffraction lines at 33.2°, 35.5°, 40.8°, 49.4°, 54.0°, 54.5°, and 62.4°, as labeled by “^” in Figure 5, correspond respectively to (104), (110), (113), (024), (116), (018), (214) planes of α-Fe_2O_3 (JCPDS file no. 89–8104).31–33 Therefore, Fe_2O_3 phase exists in nanostructures prepared with 1 at.% Fe doping and nearly matches the previously reported solubility range of Fe doping in ZnO.[27] Thus, XRD conclusion regarding formation of less prominent secondary phases ($ZnFe^2O^4$, Fe_2O_3) along with predominant $Zn_{1-x}Fe_xO$ phase, supports SEM, TEM, and EDX interpretations and hence substantiate Fe concentration dependent structural transformation of nanostructures.

Furthermore, it is noticeable that dominant reflections arise from (101) and (002) planes for all XRD spectra. In case of Fe doped ZnO nanostructures, the shifting of these peaks towards higher diffraction angle is observed, as compared to corresponding peak positions for undoped ZnO. The trend of (101) peak shifting with different Fe doping, as shown in the Figure 5(ii), is of particular interest here. The position of this peak initially shifts towards higher angle for 1 at. % Fe and achieves maximum shifting for 3 at. % Fe. Afterwards, this peak shifts backward and decreases gradually till 10 at. % Fe. This trend of variation in (101) peak shift is directly correlated with the morphological alterations in Fe incorporated ZnO nanostructures, as discussed ahead.

It is well established that the energy barrier for forming substitution atoms is smaller than that for forming interstitial atoms and hence probability of forming substitution atoms is higher than that of forming interstitial atoms.[25] This implies that Fe atoms would preferably substitute Zn atoms in ZnO so as to form, i.e., $Zn_{1-x}Fe_xO$. It is also known that the solubility of a dopant primarily depends on its valance states and corresponding ionic radii. For $Zn_{1-x}Fe_xO$ phase, Fe ions need to have a valance state of +2 in order to properly substitute Zn^{2+} ionic sites while maintaining charge neutrality. When Fe^{3+} ions coexist with Fe^{2+} ions in $Zn_{1-x}Fe_xO$, the Fe^{3+} ions are expected to distort the lattice structure to hold the charge neutrality.[34,35] The ionic radii of Fe^{2+}, Fe^{3+}, and Zn^{2+} are 0.078, 0.068, and 0.074 nm, respectively.[34] The ionic radius of Fe^{2+} is larger than that of Zn^{2+} by 5.4%, whereas that of Fe^{3+} is smaller than of Zn^{2+} by 8.1%.[24,34] When Fe^{2+} and Fe^{3+} replace Zn^{2+} substitutionally, different types and magnitudes of strain are produced due to the ionic radii difference of Fe^{2+} and Fe^{3+}.

Moreover, it is reported earlier that depending on the factors like synthesis technique, Fe dopant source (e.g., Fe_2O_3 in our case) as well as native point defect density in ZnO, the doped Fe in ZnO may exist either in the form of Fe^{2+} or Fe^{3+} or both.[34] If Fe^{2+} and Fe^{3+} coexist in ZnO, the molar ratio of Fe3+/Fe2+ will determine the type of strain. When Fe ions in ZnO exist mainly in the form of Fe^{2+}, it will lead to compression strain in the lattice and as a result XRD peak shifts towards smaller angle.[36] Whereas if Fe ion in ZnO exist mainly in the form of Fe^{3+}, it will lead to tensile strain in the lattice and hence XRD peak shifts towards higher angle.[36] In our case, shifting of (101) peak for all Fe doped nanostructures is towards higher angle as compared to undoped ZnO however, this peak shifting does not increase monotonically for 1–10 at. % Fe. Therefore, we infer that Fe^{3+} as well as Fe^{2+} ion coexists in our case. The occurrence of Fe_2O_3 phase is solely due to Fe^{3+} ions whereas the formation of $ZnFe_2O_4$ and $Zn_{1-x}Fe_xO$ phases is due to concurrence of Fe^{2+} and Fe^{3+} ions.[25,30,34,37–40]

Besides shifting, the peak broadening with increased Fe concentration was also reported earlier.[39] Owing to difference in ionic radii of Zn and Fe ions, peak broadening had been explained on the basis of grain size reduction and strain development in ZnO lattice with Fe incorporation.[30,34,39,40]

In order to examine the effect of Fe concentration on the crystal parameters of prepared nanostructures, the lattice parameters (a and c) and average crystallite sizes (D) were calculated using formula (1) and (2), respectively,

$$\mathrm{Sin}^2\theta = \frac{\lambda^2}{4}\left[\frac{4}{3}\left(\frac{h^2+hk+k^2}{a^2}\right)+\frac{l^2}{c^2}\right] \qquad (1)$$

and

$$D = \frac{0.9\lambda}{\beta\cos\theta}, \qquad (2)$$

where symbols stand for their usual meanings.[39] The calculated values are presented in Table II.

No definitive trend of variation in the calculated crystal parameters could be observed for prepared nanostructures. Slight variation in lattice constants of undoped and differently doped nanostructures could be due to Zn and Fe ionic size mismatch. The variation of average crystallite size with Fe concentration is also observed in Table II. The qualitative decrement of the grain size with Fe doping was earlier reported and attributed to the decrease in nucleation and growth rate due to higher ionic radius of Fe^{2+} as compared to Zn^{2+}.[37,39] In our case also, except for 3 at. % Fe, shrinkage in crystallite size due to Fe incorporation, as compared to that of undoped ZnO, is generally observed. However, the variation of crystallite size with different Fe concentrations does not show any definite pattern. Therefore, indefinite trend in lattice constants and crystallite size may be ascribed to size mismatch and actual concentration of Zn and Fe cations at respective stages of nanostructure evolution.[39]

TABLE II. Crystal parameters calculated for undoped and Fe doped nanostructures.

Crystal Parameters		Undoped ZnO	1%	3%	5%	7%	10%
Lattice Constants	a (Å)	3.24	3.24	3.23	3.24	3.24	3.24
	c (Å)	5.20	5.20	5.18	5.20	5.20	5.20
Crystallite size D (nm)		36	26.5	42.6	19.4	19.8	23.8

Direct evidences of morphological growth of nanostructures obtained through SEM/TEM images and formation of primary $Zn_{1-x}Fe_xO$ and secondary phases (i.e., $ZnFe_2O_4$ and Fe_2O_3) interpreted through XRD provide us sufficient information to comprehend Fe dopant dependent morphological evolution of nanostructures; and therefore, the model along with the detailed mechanism of this evolution is explicated ahead.

Model and mechanism of morphological evolution of nanostructures: The wurtzite structure of ZnO is basically comprised of four fold coordinated O^{2-} and Zn^{2+} ions, stacked alternatively along the c-axis; as shown in schematic (Figure 6(a)). ZnO has partial ionic characteristics, thus there is a net dipole moment along the c-axis. For the basal planes, the (0001) plane can be terminated with Zn [(0001) – Zn] or oxygen [(000$\bar{1}$) – O] resulting in positively and negatively charged top and bottom surfaces.[41] If the surface charges are uncompensated, the net dipole moment and the electrostatic potential increase and subsequently results the divergence of surface energy for large polar surfaces. Worth noting here is that the [0001) – Zn] surface has been reported to be chemically active, possibly due to self-catalyzed process in growth of ZnO; while the [000$\bar{1}$)-O) terminated surfaces are chemically inert.[42,43] Other commonly observed planes of {0110} and {2110} are non-polar planes which have lower surface energy compared to the polar basal plane. Furthermore, under thermodynamic equilibrium condition, the facets with higher surface energy are usually smaller in surface area; whereas the lower energy facets are larger.[41]

Morphological evolution in our case can therefore be comprehended jointly on the basis of crystal strain due to Fe^{x+} incorporation, high and low energies respectively of polar {0001} and non-polar [(2110), (0110)] surfaces.[44–46]

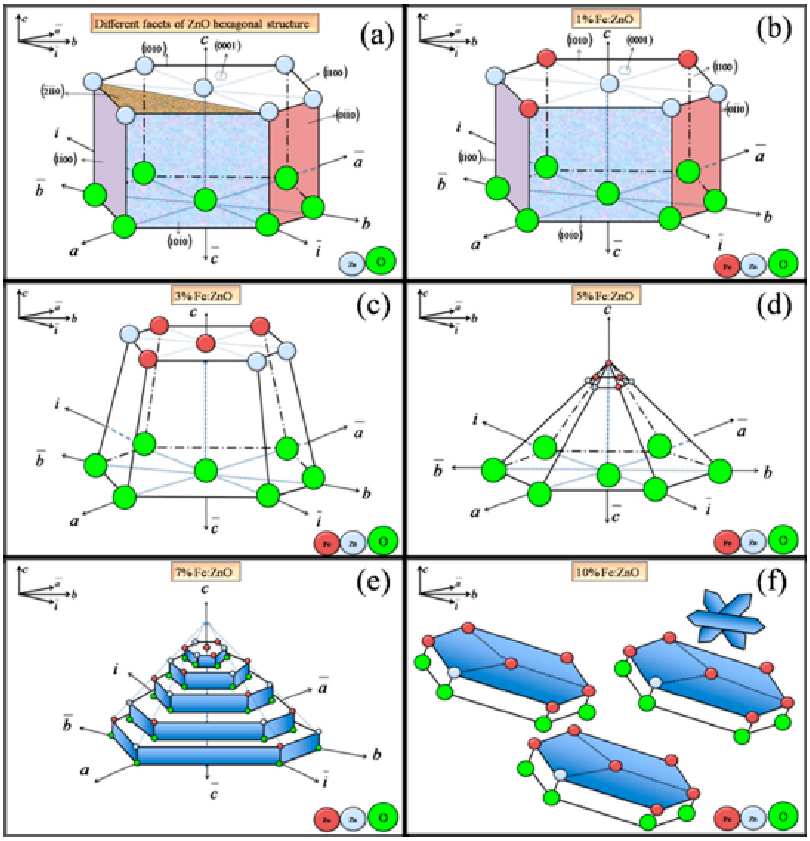

FIG. 6. Schematic depicting dopant concentration driven morphological evolution of nanostructures at successive stages: (a) Facets and ions arrangement for undoped ZnO, (b)-(f) Crystallite growth models respectively for 1, 3, 5, 7, 10 at. % Fe doped ZnO.

Based on these concepts and with the help of a schematic (Figure 6), the morphological evolution of nanostructure could be suitably explained now.

The substitution of Zn ions by Fe ions initiates with 1 at. % Fe doping (Figure 6(b)). Due to the difference in ionic radius of Fe^{x+} (x=2 or 3) and Zn^{2+}, when a large number of Fe^{x+} substitutionally replace Zn^{2+}, lattice distortion is intensified; resulting in larger strain and consequently affecting normal growth of ZnO crystals. The crystallographic anisotropy of ZnO favors anisotropic growth. This is evident through transformation of nanoparticles into hexagonal shaped nanorods for 3 at. % Fe doped ZnO (Figure 6(c)). Thus, formation of nanorods is the result of anisotropic growth of crystal along c-axis where Fe ions preferably accumulate on chemically active [(0001) – Zn] top surface (Figure 6(c)). However, with increased Fe doping (i.e., for 5 at. %), further growth of active [(0001) – Zn] top surface is not possible. In order to minimize the higher surface energy of this active polar plane, the flat surface of this plane converges; and due to the convergence of this plane, hexagonal nanorods transforms to prismatic nanocones (Figure 6(d)). Here, the hexagonal base of nanocones represents unaffected [$(000\bar{1})$-O] surface whereas the tip represents Fe substituted active [(0001) – Zn] plane (Figure 6(d)). Interestingly, this is endorsed through TEM elemental mapping analysis too; where Fe ions found to be located at the tip points of prismatic nanocones (Figure 3(d)). But, reduction of [(0001) – Zn] surface energy is not sufficient for further Fe doping (7 and 10 at. %). Therefore, with increased Fe doping, growth of low energy non-polar planes [e.g., (2110), (0110)] is essential. This is the reason behind the collapse of prismatic nanocones, as observed in Figure 1(e) and schematically shown in Figure 6(e). Finally, at 10 at.%, surface energy is further minimized for nanoflakes (Figure 1(f)) and their formation could be visualized through the slicing of nanocones, as illustrated in Figures 6(d) and 6(e).

Having deciphered the mechanism of morphological evolution and in view of coexistence of primary and secondary phases, it would be of particular interest to systematically investigate the role of different phases in vibrational and optical properties of prepared nanostructures.

Fourier transform infrared spectroscopy analysis: Since FTIR spectroscopy can uniquely reveal the details of functional groups, molecular geometry, and inter- or intramolecular interactions in a compound, we perform FTIR spectroscopy of nanostructures.[39] IR spectra can also provide information about position and valency of the ions in crystal lattice. Hence, present investigation is intended to acquire additional information about valence states and vibrational modes of prepared nanostructures.[47] In order to detect the alteration in vibrational modes at different stages of structural transformation, FTIR transmission mode spectra are recorded in 370–4000 cm^{-1} range for Fe doped ZnO nanostructures and presented in Figure 7.

To pinpoint variations in IR spectra due to Fe doping, it is imperative to identify common vibration modes due to Zn–O bonding in undoped and Fe doped ZnO. The band frequencies within 900 cm^{-1} are usually examined to detect the IR active bonding amongst inorganic elements, such as Zn–O. IR absorptions at 421 cm^{-1}, 535 cm$^{-1,}$ and 621 cm^{-1}, as shown in Figure 7, are common to all and correspond to vibrational modes of Zn–O (marked with "Δ" in Figure 7).[19,39] The appearance of these modes re-affirms formation of ZnO phase for prepared nanostructures.

Having identified Zn–O modes, we now try to detect the presences of $ZnFe_2O_4$ phase through FTIR data. Previously, XRD analysis suggested the existence of spinel $ZnFe_2O_4$ nanostructures in Fe doped ZnO for 1 at. % onwards. It is already reported that spinel zinc ferrite exhibits four basic IR active modes (namely v1, v2, v3, v4).[48]

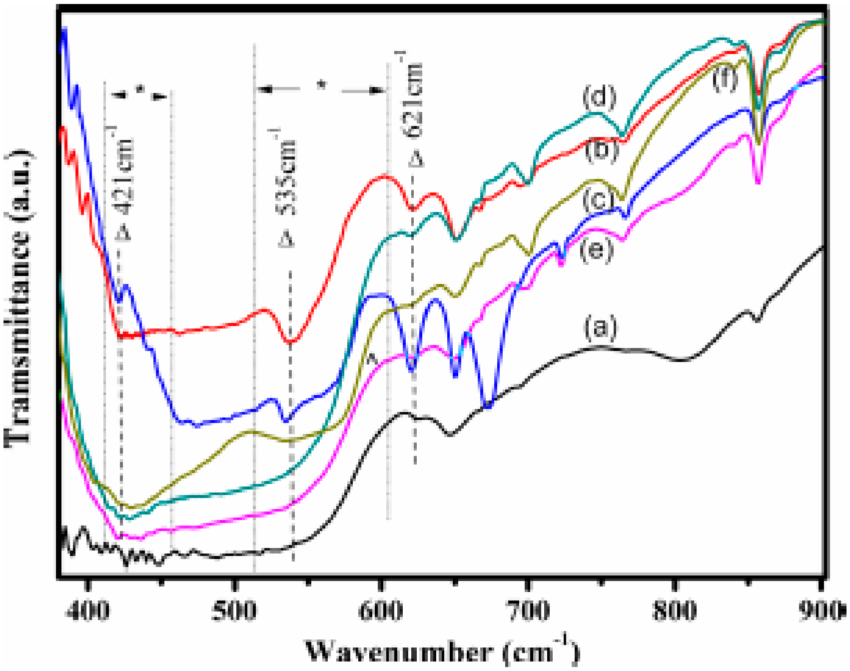

FIG. 7. FTIR spectra of (a) undoped, (b)1 at. %, (c) 3 at. %, (c) 5 at. %, (d) 7 at. %, and (e) 10 at. % Fe-doped ZnO nanostructures. The peak positions pertaining to $Zn_{1-x}Fe_xO$, $ZnFe_2O_4$ and Fe_2O_3 phases are labeled respectively through symbols Δ, *, and ^.

The high frequency bands (v1 and v2) are very sensitive to change in interaction between oxygen and cations in tetrahedral and octahedral positions and frequently appear respectively in the range of 540–600 cm^{-1} and 400–450 cm^{-1}.[48] The low frequency band v3 appear close to 330 cm^{-1} and v4 varies from 164–168 cm$^{-1.}$ The bands v3 corresponds to divalent as well as oxygen and □4 corresponds to thermal vibrations.[48]

Further, the high frequency band around 540 cm^{-1} and the low frequency band around v2 around 417 cm^{-1} was attributed respectively to tetrahedral and octahedral groups.[48] We too observe 400–450 cm^{-1} and 540–600 cm^{-1} bands in undoped as well as Fe doped ZnO nanostructures (marked by dotted lies and "*" in Figure 7). In present study, IR modes for zinc ferrite may lie in the expected range but due to coincidence of 421 cm^{-1} and 512 cm^{-1} modes of Zn–O, the bands of ZnO and ZnFe2O4 cause aggregated broadening of peaks. The peak at 1257 cm^{-1} (earlier reported at 1257 cm^{-1} (Ref. 48) was reported due to overtones (present in our case too but not shown in Figure 7). However, the low frequency bands v3 and v4 did not appear in our spectrum since these lie beyond the range of our FTIR instrument. Thus, presence of $ZnFe_2O4$ is shadowed by concurring ZnO modes.

Having analyzed IR modes of ZnO and $ZnFe_2O_4$ phases, we attempt to probe IR modes of Fe_2O_3, since existence of this phase was revealed already through XRD results. In this context, intense absorption peaks at ~624 cm-1 and ~596 cm^{-1} related to stretching modes of Fe–O bond are already reported for pure Fe–O samples.[49] In our case, a mode at 621 cm^{-1} is vividly observed for all samples. Though, coinciding with ZnO modes, this mode indicates the formation of Fe–O bonds for Fe doped ZnO nanostructures. [49] Thus, FTIR analysis endorses XRD results, which suggested the formation of Fe_2O_3 and $ZnFe_2O_4$ secondary phases, in addition to primary $Zn_{1-x}Fe_xO$ phase of nanostructures. However, no distinct mode due to Fe-O bond or Zn-Fe-O linkage could be detected. Owing to the fundamental difference in detection schemes of FTIR and Raman spectroscopies, Raman spectroscopy could acquire additional information, unattained earlier through FTIR analysis. Aiming to detect Fe-O and Zn-Fe-O Raman active modes, distinguishable from commonly observed Zn-O modes, we attempt micro-Raman spectroscopy (μRS) of prepared samples.

Micro-raman spectroscopy analysis: Raman spectroscopy is considered to be powerful nondestructive technique to study the crystalline quality, structural disorder and defects in the host lattice.[39] In particular, IRS has proven to be a very sensitive technique to detect local structural changes due to incorporation of transition metal ions into ZnO host lattice.[39] To reveal the vibrational properties of smaller nanoparticles, it is crucial to study and compare the same with their bulk counterpart. Due to quantization of energy states, shifting and broadening of modes is expected when a material transits from bulk to nanometric size. In order to investigate vibrational properties of 1 at. %, 5 at. %, and 10 at. % Fe doped ZnO nanostructures and accordingly, influence of doping on their phase and microscopic structure, we recorded Raman spectra in the range of 89–800 cm^{-1}, as presented in Figure 8.

To understand the lattice changes occurring in Fe doped ZnO, we need to first discuss details of group theory of wurtzite structure of ZnO. Hexagonal structure of ZnO belongs to the space group $C\frac{4}{3v}$, with two formula units per primitive cell, where all atoms occupy C_{3v} sites.[19] The optical phonons at the Brillouin zone center belong to irreducible representations: $T_{opt}=A_1+2B_1+E_1+2E_2$ Modes of symmetry A_1, E_1, and E_2 are Raman active; A_1 and E_1 are IR active too, whereas $2B_1$ is a silent mode.[19]

Both A1 and E1 are polar modes and split into transverse optical (TO) and longitudinal optical (LO) phonons with different frequencies due to macroscopic electric fields associated with the LO phonons.[19] The short-range inter-atomic forces cause anisotropy. That is why A_1 and E_1 modes have different frequencies. As the electrostatic forces dominate the anisotropy in the short-range forces, the TO–LO splitting is larger than the A_1–E_1 splitting.[19] For the lattice vibration, A_1 atoms move parallel to the c-axis and for E_1 perpendicular to c-axis.[19] Two non-polar Raman active modes are often assigned as $E_{2}^{(1)}$ (low) and $E_{2}^{(1)}$ (high). [19] The low frequency E_2 mode is predominantly associated with the non-polar vibration of the heavier Zn sub-lattice, while the highfrequency E_2 mode involves predominantly the displacements of lighter oxygen atoms.[19] All these modes have been often reported in the Raman scattering spectra of bulk ZnO.[50–52] These various Raman active modes of ZnO are assigned in Figure 8.

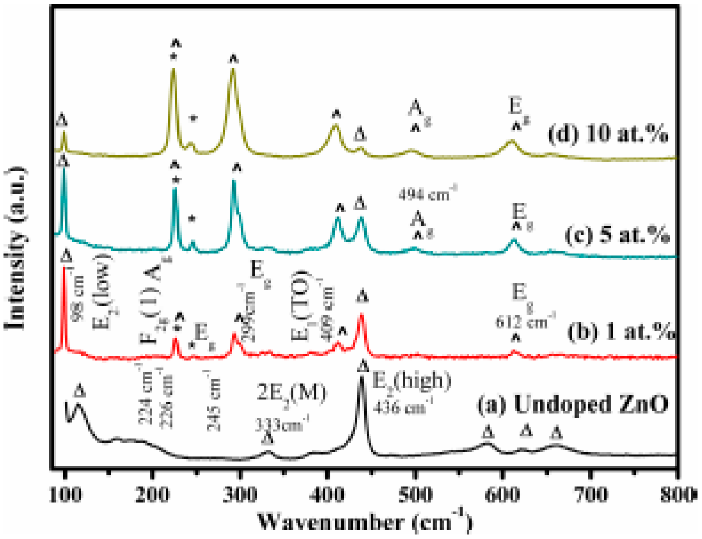

FIG. 8. Micro-Raman spectra of (a) undoped, (b) 1 at. %, (c) 5 at. %, and (d) 10 at. % Fe doped ZnO nanostructures. The peak positions pertinent to $Zn_{1-x}Fe_xO$, $ZnFe_2O_4$ and Fe_2O_3 phases are labeled respectively through symbols Δ, *, and ^.

The modes at 115 cm^{-1} for undoped ZnO, red shifted to 98 cm^{-1} for Fe doped ZnO, correspond to E_2(low) mode of ZnO.19 The vibrational mode of 330 cm^{-1} for undoped ZnO, shifted to 333 cm^{-1} for Fe doped ZnO, originates basically via two phonon process of ZnO scattering from K–M–R Brillouin zone around 160 cm^{-1} and hence referred as $2E_2$(M) mode in bulk and quantum dots of ZnO.[19] Mode at 438 cm^{-1} corresponding to E_2(high) in undoped ZnO shifts to 436 cm^{-1} for Fe doped ZnO. The vibration mode at 661 cm^{-1} is observed for undoped and doped nanostructures. In accordance with published report, it is an intrinsic mode of ZnO, related to oxygen vacancies, zinc interstitials, antisite oxygen, etc.[19] However, a vibrational mode around 580 cm^{-1} is observed only for undoped ZnO. This region earlier reported for E_1 (LO) and A1 (LO) Raman modes of ZnO.[19] Another weak Raman mode at 621 cm^{-1} is also observed only for undoped ZnO. To the best of our knowledge, there is no discussion of this mode except its association with multi-phonon processes, presumably occurring for phonon wave vectors considerably removed from the centre of the Brillouin zone.19 Absence of 580 and 621 cm^{-1} modes for all Fe doped samples indicates that doping of Fe in ZnO causes alteration of pure ZnO lattice so as to form doped $Zn_{1-x}Fe_xO$ phase. Thus, demarcation of $Zn_{1-x}Fe_xO$ phase from ZnO phase, which was earlier suggested through XRD analysis, is substantiated now through micro-Raman analysis.

Having explained basic modes of ZnO and $Zn_{1-x}Fe_xO$ phases, we now attempt to detect Raman modes of $ZnFe_2O_4$ phase. The spinel AB_2O_4 phase of $ZnFe_2O_4$ possesses a cubic structure that belongs to the space group $O\frac{7}{h}$ [50] Its full unit cell contains eight formula units and primitive cell contains two formula units. The optical phonons at C-point of the Brillouin zone belong to irreducible representations: $T_{opt} = A_{1g} + E_g + F_{1g} + 3F_{2g} + 2A_u + 2E_u + 4F_{1u} + 2F_{2u.}$ There are five first-order Raman active modes, A_{1g}, $E_{g,}$ and $3F2_g$ whereas mode F_{1u} is IR active.50 In cubic spinels, including ferrites, the modes above 600 cm^{-1} mostly correspond to motion of oxygen atoms in tetrahedral AO4 group.[50] The other lower frequency modes represent the characteristic of octahedral BO_6 sites.[50] Respective Raman active modes of $ZnFe_2O_4$ are assigned in Figure 8. The $F\frac{(1)}{2g}$ mode of $ZnFe_2O_4$ phase at 224 cm^{-1} (represented by "*") is prominently observed for Fe doped samples only. Moreover, intensity of this mode proportionally increases with Fe concentration and hence suggests that $ZnFe_2O_4$ phase formation gets prominent with higher Fe doping.[39,50]

At last, we look into Raman signatures of Fe_2O_3 phase, which was observed in XRD data of Fe doped nanostructures. Although for this phase, low intensity diffraction lines were observed for low Fe concentration (i.e., 1 and 3 at. %) and with increased doping (i.e., 5 at. % onwards) Fe_2O_3 phase becomes prominent, as evident through the intensity enhancement and emergence of pertinent diffraction lines. To further reveal the vibrational properties of Fe2O3 phase at different doping concentrations, we examine basic Raman modes of Fe_2O_3. As per group theory, Fe_2O_3 crystallizes in the rhombohedric (trigonal) system with space group D_{3d}^{6}[50] Primitive unit cell of Fe_2O_3 contains two formula units. The optical phonons at the C-point of the Brillouin zone belong to irreducible representations $T=2A_{1g}+2A_{1u}+3A_{2g}+2A_{2u}+5E_g+4E_u$. Out of these, $2A_{1g}$ and $5E_g$ are Raman active modes. $2A_{2u}$ and $4E_u$ modes are IR active.[50] Raman modes at 226 cm^{-1} (Ag), 299 cm^{-1} (E_g), 494 cm^{-1} (A_g), 612 cm^{-1} (Eg) (marked with “^” in Figure 8) are vividly observed for all Fe doped nanostructures and therefore, in line with XRD results, Fe_2O_3 phase is being formed due to unsubstituted Fe in ZnO nanolattice.[50]

As Fe doping increases, the various Raman modes of ZnO become broad, relatively less intense, and red shifted. For example, the most intense signature peak of wurtzite structure around 437cm^{-1} could be assigned to high frequency E_2 mode.[39]

The pronounced broadening and weakening of this non-polar E_2(high) mode at 436cm^{-1} for Fe-doped ZnO samples, as compared to undoped ZnO, is the consequence of structural defect formation and local lattice distortions, induced by Fe substitution.39

This is in good agreement with previous report and reveals that local symmetry in Fe doped nanocrystals is different from that of undoped ZnO, though the hexagonal crystal structure retains.[39] Thus, micro-Raman analysis is in good agreement with XRD and FTIR analyses to establish the substitution of Fe in ZnO lattice and but more importantly substantiates the existence of $ZnFe_2O_4$ and Fe_2O_3 phases concurring with $Zn_{1-x}Fe_xO$ phase.

Having ascertained structural phases and vibrational properties, we now attempt to investigate the possible influence of Fe doping on intrinsic optical processes of ZnO nanostructures. In order to study the complementary processes of electronic absorption and radiative recombination, UV-visible absorption and Photoluminescence spectroscopies are employed respectively.

UV-visible spectroscopy analysis

Optical properties of ZnO particles become increasingly important as the size of particles is reduced to nanoscale.[10,11,19,53] In order to examine the effects of Fe impurity on electronic absorption processes of ZnO, we performed UV-visible spectroscopy. To avoid the influence of surrounding medium, for example, aqueous medium in case of colloidal particles, we preferred UV-visible absorption spectroscopy of powder form of samples. Figure 9 shows UV–visible absorption spectra of Fe doped ZnO nanopowders in diffused reflectance mode. In this regard, the model put forward by Kubelka-Munk (K-M) is based on the assumption that diffuse reflectance arises from absorption and scattering of light through surface.[54–56] K-M model holds well when particle size is comparable to, or smaller than the wavelength of the incident light. In such situation the diffuse reflection, no longer allows to separate the contributions of reflection, refraction, and diffraction implying that scattering takes place.[55] In the limiting case of an infinitely thick sample, thickness and sample holder have no influence on the value of reflectance (R). In this case, the K-M equation becomes

$$F(R_\infty) = \frac{(1 - R_\infty)^2}{2R_\infty}, \qquad (3)$$

$F(R_\infty)$ is the so called remission or K-M function, where $R_\infty = R_{sample}/R_{standard.}$

For parabolic band structure, the band gap (Eg) and absorption coefficient (∞) of a direct band gap semiconductor, are related through equation[55]

$$\alpha h\nu = C_1(h\nu - E_g), \qquad (4)$$

where ∞ is the linear absorption coefficient of the material, ht is the photon energy, and C_1 is a proportionality constant. When the material scatters in perfectly diffuse manner and considering the constant K-M scattering coefficient with respect to wavelength, we obtain the expression

$$[F(R_\infty)h\nu]^2 = C_2(h\nu - E_g). \qquad (5)$$

Therefore, obtaining F (R∞) from Eq. (3) and plotting the $[F(R\infty)\ hv]^2$ against hv, the band gap Eg gap Eg of a powder sample can be extracted [54] Since we acquired the nanopowder form of direct band gap semiconductor ZnO for which surface to volume ratio is high, application of aforesaid K-M model is suitable to study the optical absorption processes and band gap of Fe doped ZnO nanostructures.

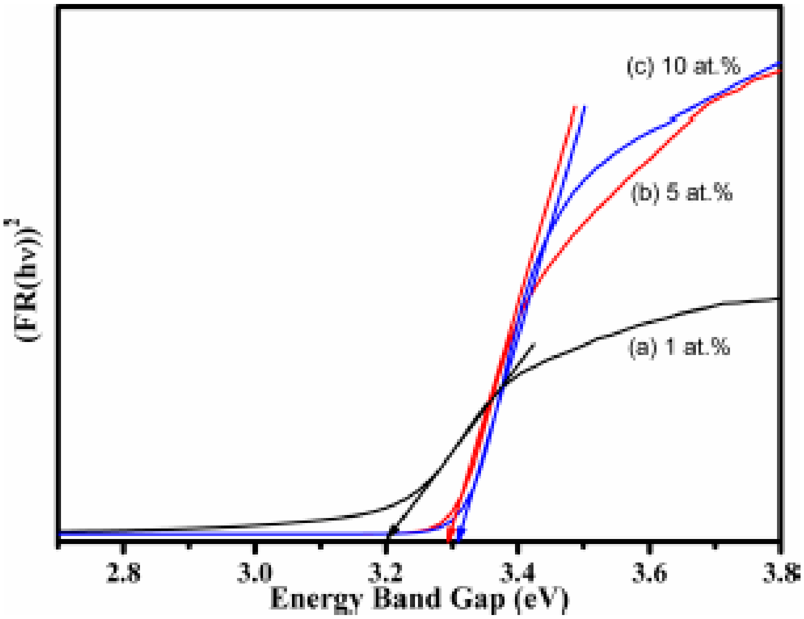

FIG. 9. Spectra for band gap calculation of (a) 1 at. %, (b) 5 at. %, and (c) 10 at. % Fe doped ZnO nanostructures applying Kubelka-Munk method.

The band gap estimated through K-M method found to be 3.21, 3.29, and 3.32 eV respectively for 1 at. %, 5 at. %, and 10 at. % Fe doped ZnO nanostructures. Thus, band gaps for prepared samples found to be higher than that of bulk ZnO (i.e., 3.2 eV).[10] The increase in band gap represents the blue shift in band gap from its bulk counterpart. The increase in the band gap with decrease in the crystallite size is earlier attributed to size confinement effects.[10,57,58] But, particle sizes in our case are much bigger and hence the band gap shifts cannot be assigned to size quantization.

Earlier blue shift was observed for low Fe doping (say <1.5 at. %), whereas little red shift was observed at higher doping percentages. This increase in band gap was elucidated through Burstein-Moss band filling effect.[39] It is well known that ZnO is a n-type material and when doped with Fe, the Fermi level gets inside the conduction band by nn.[39] Since the states below nn in the conduction band are filled, the absorption edge should cause the broadening of band gap.[39] Furthermore, small red shift of band edge was observed for higher doping of Fe in nanoparticles.[39] This was interpreted as sp–d exchange interactions between the band electrons of ZnO and the localized d electrons of the Fe-ions.[39] This interaction, in addition to Burstein-Moss effect, arises due to replacement of Zn^{2+} ions by Fe^{2+} ion. The s–d and p–d exchange interactions eventually lead to a negative and a positive correction respectively to the conduction band and the valence band edges and hence, resulting in the band gap narrowing.[39] The increase in band gap values with increased Fe concentration, as observed in our case, is suggestive of the inhibition of crystal growth via incorporation of dopant species.[59]

Therefore, besides crystal size effect, the variation in the band gap energy could also be caused through dopant incorporation. [59] Though the results of band gap variation were explained in terms of the distortion of the host lattice and generation of defects, these factors would not necessarily play a major role in the determination of the band gap energy due to negligible variation in lattice constants of synthesized nanostructures.[58] In view of aforesaid various interpretations, widening of the band gap in prepared Fe doped ZnO nanostructures could more appropriately be attributed to the joint effect of two phenomena; first, sp-d exchange interaction between valence band electrons and localized d electrons of substituting Fe ions; and second, the Burstein-Moss band filling effect arising due to Fe doping.[59] Since widening of bang gap and doping of nanostructures may also introduce various defect and discrete energy states, it is therefore crucial to identify the radiative recombination transitions occurring in Fe doped ZnO nanostructures. Aiming this, we also perform photoluminescence spectroscopy of prepared nanostructures.

Photoluminescence spectroscopy analysis:

The size confinement and surface effects such as defects, density of semiconductor nanoparticles, does not only increase the band gap but also influences various optical transitions, such as luminescence.[39] The room temperature PL spectra of undoped and 1 at. %, 5 at. %, 7 at. %, and 10 at. % Fe doped ZnO nanostructures were acquired employing an excitation line of 250 nm, and presented in Figure 10.

A quick glance at PL spectra clearly indicates that undoped as well as Fe doped ZnO exhibit common regions of photoluminescence. As the first PL region, all spectra exhibit prominent near UV emission around 390 nm. Various PL emissions are observed in the visible spectral region. Among such emissions, the first and most intense is the indigo emission centered at 442 nm. Afterwards, a wide range of visible emission for ZnO and Fe doped ZnO appears in the form of a broad PL peak of 500–685 nm. A broad region centered on 580 nm corresponds to the “green-red” range of visible spectrum. We analyze all these emissions in forthcoming sections.

As per published literature, photoluminescence in Fe doped ZnO at 523 nm and 632 nm correspond respectively to green and orange emissions.30 Blue emission at 468 nm, 440 nm and violet emissions at 412 nm were also reported earlier in Fe doping, together with the quenching of green and orange emissions.[30] In the same report, it was found that with Fe doping in ZnO not only the overall PL intensity reduced significantly but some additional bands were also observed with the pre-existing green and orange bands.[30] Our PL results are in good agreement with literature report, as we also observe a broad hump from 500–685 nm for green-orange-red region with peak at 580 nm. Interestingly, in line with previous findings, we not only observe the blue emission (390 nm and 442 nm) for our samples but more importantly notice the gradual quenching of UV, violet, green, and orange emissions with increase in Fe concentration.[30]

Having observed aforesaid several PL emissions and most importantly the gradual quenching of all modes with increased Fe doping, we now attempt to interpret the origin and quenching of these PL emissions. Various models and mechanisms are responsible for these emissions.[30,60–64] Most of the emission bands observed in our case could be explained on the basis of previously reported mechanisms.[30]

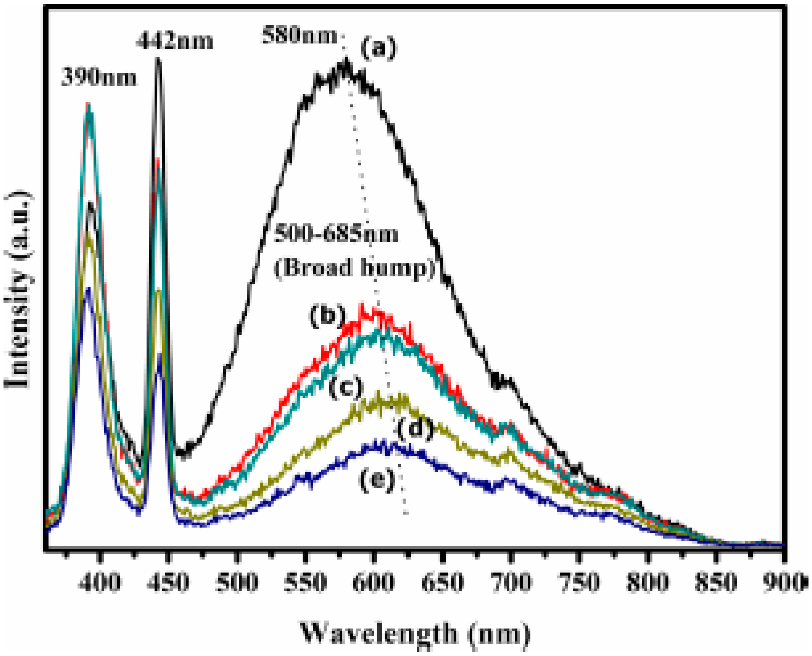

FIG. 10. PL spectra of (a) undoped, (b) 1 at. %, (c) 5 at. %, (d) 7 at. %, and (e) 10 at. % Fe-doped ZnO nanostructures.

The green-orange emissions around 500–685 nm is considered to be originated from doubly ionized oxygen vacancies (O^{2-}), which act as traps for photo-generated holes.[61] It is also suggested earlier that the rate of hole trapping is faster and efficient when surface to bulk ratio is high for nanometric size ZnO particles.[30] But doping of Fe could actually result in increase of particle size due to relatively coarser size $ZnFe_2O_4$ particles and hence decrease in surface to volume ratio leads to an overall decrease in surface trapping process and eventually decreases the green-orange PL intensity.[30]

Based on reported X-ray photon spectroscopic (XPS) investigations, formation of $ZnFe_2O_4$ additional phase suggested that Fe is incorporated in the ZnO matrix in a state close to Fe^{3+}.30 XPS measurements had verified Fe^{3+} to be selectively bonded to electrons in singly ionized oxygen vacancies (O^{-}), which implied that the probability of recombination of electrons and holes in the valence band reduces with increased Fe doping and hence, intensity of green emission decreases.[60] Thus, the occurrence of green-orange band and the gradual decrease of its intensity are in excellent agreement with published model and mechanisms of photoluminescence in undoped and Fe doped ZnO nanostructures.[30,60,62]

Finally, we explicate the abovementioned similar issues for blue/indigo emissions, as noticed in our PL spectra. In this context, blue emissions around 468 nm and 440 nm were assigned earlier to intrinsic defects particularly to interstitial zinc, which resulted from non-stoichiometric ZnO favouring the formation of additional phase of $ZnFe_2O_4$.[63] Therefore, 442 nm emissions in our case could be attributed to interstitial zinc. On the basis of previous report, two more important points could be made through our PL analysis. First, with increase of Fe concentration, the overall PL has significant contribution of $ZnFe_2O_4$ phase, the presence of which is already established from XRD results. Second, the UV band around 390 nm, the intensity of which is more intense than the intensity of orange-green band of respective samples, is most probably due to the radiative defects. These emissions are related to the interface traps existing at the grain boundaries of ZnO and $ZnFe_2O_4$ phases and result from the radiative transitions between these trap levels and the valence band.[64] Thus, various significant optical processes of undoped and Fe doped ZnO nanostructures were revealed by PL study. More importantly, the formation of $ZnFe_2O_4$ phase and related intricate details of structural and optical processes were endorsed through PL analysis.

Conclusion

In summary, we attempted to incorporate 1–10 at. % Fe doping into ZnO nanostructures. Depending on dopant concentration, prepared nanostructures exhibit different morphologies of nanoparticles, nanorods, nanocones, and finally nanoflakes. Dopant concentration dependent morphological evolution was systematically studied through analysis of structural, vibrational, and optical properties. The shape, size, and stiochiometry of prepared nanostructures were ascertained through electron microscopy and x-ray spectroscopic measurements. The XRD analysis reveals the formation of $ZnFe_2O_4$ and Fe_2O_3 secondary phases in addition to the primary phase of $Zn_{1-x}Fe_xO$. A model as well as mechanism details were explicated to comprehend the dopant concentration dependent morphological evolution. Vibrational modes of metal oxygen bondings were analyzed through FTIR data. However, IR active vibrational modes of Fe-O or Zn-Fe-O linkage could not be distinguished due to concurring dominant modes of Zn-O. Micro-Raman spectroscopic analysis not only identifies fundamental Raman modes of Zn-O but more crucially distinctly demonstrates Fe-O mode of Fe_2O_3 and Zn-Fe-O mode due to $ZnFe_2O_4$ phase. Substantiating the XRD analysis, Raman analysis establishes the onset of formation of Fe_2O_3 and $ZnFe_2O_4$ secondary phases along with primary $Zn_{1-x}FexO$ phase at 1 at. % Fe doping. Moreover, in line with XRD results, Raman analysis vividly demonstrates gradual prominence of secondary phases with increased Fe doping concentration (5 at. % onwards). The blue shift in band gap energy of Fe doped nanostructures, as estimated through UV-visible analysis, could be attributed to joint effect of sp-d exchange interaction and Burstein-Moss band filling. Similar to undoped ZnO, various visible PL emissions were observed for Fe doped ZnO nanostructures. Interestingly, systematic quenching of PL emissions with enhanced Fe doping was observed and interpreted on the basis of decrease in surface-to-volume ratio due to relatively coarser size $ZnFe_2O_4$ particles with gradual increase of Fe doping concentration.

Acknowledgments

N.G. acknowledges the Advanced Materials Research Division, JIIT Noida. A.S. gratefully acknowledges Department of Science and Technology (DST), India for INSPIRE fellowship.

References

1J. A. Rodriguez and M. Fern□andez-Garc□ıa, Synthesis, Properties, and Applications of Oxide Nanomaterials (John Wiley & Sons Inc., Hoboken, New Jersey, 2007).

2B. P. Vinayan and S. Ramaprabhu, J. Mater. Chem. A 1, 3865 (2013).

3Y. Matsumoto, M. Murakami, T. Shono, T. Hasegawa, T. Fukumura, M. Kawasaki, P. Ahmet, T. Chikyow, S. Koshihara, and H. Koinuma, Science 291, 854 (2001).

4G. Filipicˇ and U. Cvelbar, Nanotechnology 23, 194001 (2012).

5€U. €Ozg€ur, Y. I. Alivov, C. Liu, A. Teke, M. A. Reshchikov, S. Do□gan, V. Avrutin, S.-J. Cho, and H. Morkoc¸, J. Appl. Phys. 98, 041301 (2005).

6Z. L. Wang, J. Phys.: Condens. Matter 16, R829 (2004).

7J. G. Lu, Z. Z. Ye, J. Y. Huang, L. P. Zhu, B. H. Zhao, Z. L. Wang, and Sz. Fujita, Appl. Phys. Lett. 88, 063110 (2006).

8A. Segura, J. A. Sans, F. J. Manjo□n, A. Mun~oz, and M. J. Herrera-Cabrera, Appl. Phys. Lett. 83, 278 (2003).

9J. Yang, X. Liu, L. Yang, Y. Wang, Y. Zhang, J. Lang, M. Gao, and B. Feng, J. Alloy Compd. 477, 632 (2009).

10N. Goswami and D. K. Sharma, Physica E 42, 1675 (2010).

11A. Sahai and N. Goswami, Physica E 58, 130 (2014).

12A. Sahai and N. Goswami, Ceram. Int. 40, 14569 (2014).

13Z. Yan, Y. Ma, D. Wang, J. Wang, Z. Gao, L. Wang, P. Yu, and T. Song, Appl. Phys. Lett. 92, 081911 (2008).

14R. Wahab, S. G. Ansari, Y. S. Kim, H. K. Seo, G. S. Kim, G. Khang, and H.-S. Shin, Mater. Res. Bull. 42, 1640 (2007).

15H. Morkoc¸ and €U. €Ozg€ur, Zinc Oxide: Fundamentals, Materials and Device Technology (John Wiley & Sons, Federal Republic of Germany, 2008).

16S. R. Lingampalli, U. K. Gautam, and C. N. R. Rao, Energy Environ. Sci. 6, 3589 (2013).

17L. J. Brillson and Y. Lu, J. Appl. Phys. 109, 121301 (2011).

18W. J. E. Beek, M. Wienk, and R. A. J. Janssen, Adv.Mater. 16, 1009 (2004).

19N. Goswami and A. Sahai, Mater. Res. Bull. 48, 346 (2013).

20G. Glaspell, P. Dutta, and A. Manivannan, J. Clust. Sci. 16, 523 (2005).

21M. A. Shafique, S. A. Shah, M. Nafees, K. Rasheed, and R. Ahmad, Int. Nano Lett. 2, 31 (2012).

22D. P. Gosain, K. L. Bhatia, G. Parthasarathy, and E. S. R. Gopal, Key Eng. Mater. 13–15, 351 (1987).

23K. Chen, Q. Hou, X. Dong, H. Zhang, Y. Li, H. Liu, Y. Huang, and L. Qi, J. Phys.: Conf. Ser. 430, 012077 (2013).

24S. Kar, S. Biswas, S. Chaudhuri, and P. M. G. Nambissan, Nanotechnology 18, 225606 (2007).

25F. Ahmed, S. Kumar, N. Arshi, M. S. Anwar, and B. H. Koo, Cryst. Eng. Comm. 14, 4016 (2012).

26S. K. Mandal, A. K. Das, T. K. Nath, and D. Karmakar, Appl. Phys. Lett. 89, 144105 (2006).

27B. Alem□an, Y. Ortega, J. □A. Garc□ıa, P. Fern□andez, and J. Piqueras, J. Appl. Phys. 110, 014317 (2011).

28G. Oskam, J. Sol–Gel Sci. Technol. 37, 161 (2006).

29S. Steinfel, A. V. Gleich, and U. Petschow, Nanotechnologies Hazards and Resource Efficiency (Springer Verlag, London, 2007).

30A. K. Srivastavaa, M. Deepa, N. Bahadur, and M. S. Goyat, Mater. Chem. Phys. 114, 194 (2009).

31E. Darezereshki, F. Bakhtiari, M. Alizadeh, A. Behradvakylabad, and M. Ranjbar, Mater. Sci. Semicond. Proc. 15, 91 (2012).

32L. Yang, Y. Liang, H. Chen, L. Kong, and W. Jiang, Bull. Mater. Sci. 31, 919 (2008).

33J.-R. Jeong, S.-J. Lee, J.-D. Kim, and S.-C. Shin, Phys. Status Solidi B

241, 1593 (2004).

34S. M. Salaken, E. Farzana, and J. Podder, J. Semicond. 34, 073003 (2013).

35K. J. Kim and Y. R. Park, J. Appl. Phys. 96, 4150 (2004).

36J. T. Luo, Y. C. Yang, X. Y. Zhu, G. Chen, F. Zeng, and F. Pan, Phys. Rev. B 82, 014116 (2010).

37A. K. Mishra and D. Das, Mater. Sci. Eng., B 171, 5 (2010).

38J. Cui, Q. Zeng, and U. J. Gibson, J. Appl. Phys. 99, 08M113 (2006).

39S. Kumar, S. Mukherjee, R. K. Singh, S. Chatterjee, and A. K. Ghosh, J. Appl. Phys. 110, 103508 (2011).

40W.-H. Zhang, W.-D. Zhang, and J.-F. Zhou, J. Mater. Sci. 45, 209 (2010).

41X. Y. Kong and Z. L. Wang, Appl. Phys. Lett. 84, 975 (2004).

42V. Staemmler, K. Fink, B. Meyer, D. Marx, M. Kunat, S. Gil Girol, U. Burghaus, and Ch. W€oll, Phys. Rev. Lett. 90, 106102 (2003).

43Z. L. Wang, X. Y. Kong, and J. M. Zuo, Phys. Rev. Lett. 91, 185502 (2003).

44Z. W. Pan, Z. R. Dai, and Z. L. Wang, Science 291, 1947 (2001).

45Y. Dai, Y. Zhang, Y. Q. Bai, and Z. L. Wang, Chem. Phys. Lett. 375, 96 (2003).

46Z. R. Tian, J. A. Voigt, J. Liu, B. Mckenzie, and M. J. Mcdermott, J. Am. Chem. Soc. 124, 12954 (2002).

47M. A. Amer, Phys. Status Solidi A 151, 205 (1995).

48P. Dasa, A. Duttab, A. Bhaumikb, and C. Mukhopadhyay, Green Chem. 16, 1426 (2014).

49Z. R. Marand, N. Shahtahmasbi, M. R. Roknabadi, M. Hosseindokht, M. Bagheri Mohagheghi, M. H. R. Farimani, and R. Etefagh, in Proceedings of the 4th Inter. Conference on Nanostructures (ICNS4) (2012), p. 211.

50N. Romcevic, R. Kostic, M. Romcevic, B. Hadzic, I. Kuryliszyn-Kudelska, W. Dobrowolski, U. Narkiewicz, and D. Sibera, Acta Phys. Polon. A 114, 1323 (2008).

51N. Ashkenov, B. N. Mbenkum, C. Bundesmann, V. Riede, M. Lorenz, D. Spemann, E. M. Kaidashev, A. Kasic, M. Shubert, and M. Grundmann, J. Appl. Phys. 93, 126 (2003).

52E. F. Venger, A. V. Melnichuk, L. Lu. Melnichuk, and Y. A. Pasechuk, Phys. Status Solidi B 188, 823 (1995).

53L. Mart□ınez, Y. Kumar, D. Mayorga, N. Goswami, and V. Agarwal, Superlatt. Microsturct. 67, 72 (2014).

54P. Kubelka and F. Munk, Z. Tech. Phys. 12, 593 (1931).

55A. E. Morales, E. Sanchez Mora, and U. Pal, Revista Mexicana De F0Isica S 53, 18 (2007).

56J. I. Pankove, Optical Processes in Semiconductors (Dover Publications, New Jersey, 2010).

57G. Dresselhaus, J. Phys. Chem. Solids 1, 14 (1956).

58K.-F. Lin, H.–M. Cheng, H.–C. Hsu, L.–J. Lin, and W.–F. Hsieh, Chem. Phys. Lett. 409, 208 (2005).

59A. P. Palomino, O. P. Perez, R. Singhal, M. Tomar, J. Hwang, and P. M. Voyles, J. Appl. Phys. 103, 07D121 (2008).

60S. Baek, J. Song, and S. Lim, Physica B 399, 101 (2007).

61A. V. Dijken, E. A. Meulenkamp, D. Vanmaekelbergh, and A. Meijerink, J. Lumin. 90, 123 (2000).

62A. V. Dijken, E. A. Meulenkamp, D. Vanmaekelbergh, and A. Meijerink, J. Lumin. 87, 454 (2000).

63Z. Fang, Y. Wang, D. Xu, Y. Tan, and X. Liu, Opt. Mater. 26, 239 (2004).

64B. J. Jin, S. Im, and S. Y. Lee, Thin Solid Films 366, 107 (2000).